Energies of ultrarelativistic electrons produced by an oblique shock wave

Naoki Bessho and Yukiharu Ohsawa
Department of Physics, Nagoya University, Nagoya 464-8602, Japan

(Received 11 April 2000; accepted 6 July 2000)

Production of ultrarelativistic electrons in an oblique magnetosonic shock wave is studied theoretically and numerically. First, the structure of the oblique shock wave is analytically discussed on the basis of a relativistic, two-fluid model. Then, by use of the field strengths thus obtained, the maximum energy of accelerated electrons is calculated as a function of the propagation speed and angle of the shock wave. Next, a one-dimensional, relativistic, electromagnetic, particle simulation code is used to further investigate the shock propagation and associated electron acceleration. Lorentz factors of accelerated electrons can exceed 100. Detailed comparisons are made between the theoretically predicted field strengths and electron energy and those obtained by the simulations. © *2000 American Institute of Physics.* [S1070-664X(00)04210-5]

I. INTRODUCTION

The particle acceleration has been one of the major issues in plasma physics. In an attempt to reduce the size of future particle accelerators, Tajima and Dawson proposed a beat-wave accelerator in 1979.[1] Since then, various kinds of plasma-based accelerators have been investigated by computer simulations and laboratory experiments[2] (and references therein). On the other hand, it has been long known that high-energy particles are produced in astrophysical plasmas. Observations show that in solar flares ions can be accelerated to 1–10 GeV,[3] while electrons can be accelerated to several tens of mega-electron-volts.[4–6] Supernova remnants can produce electrons with energies $\sim 100\,\mathrm{TeV}$.[7–9]

Mechanisms of particle acceleration in astrophysical plasmas have usually been discussed in terms of stochastic processes, such as Fermi acceleration,[10–12] except for a few models.[13] Recently, however, it has been recognized by self-consistent simulations that particles can be accelerated to high energies in a large-amplitude plasma wave with coherent structure.

Indeed, particle simulations have revealed that there are several different such mechanisms of ion acceleration in magnetosonic shock waves (or pulses). They are, for instance, proton acceleration by the longitudinal electric field,[14–22] heavy ion acceleration by the transverse electric field,[23,24] and enhanced acceleration of energetic ions.[25,26]

Furthermore, quite recently, it has been shown by particle simulations that shock waves propagating obliquely to a magnetic field can produce electrons with ultrarelativistic energies.[27,28] In this phenomenon, some of the electrons are reflected near the end of a large-amplitude pulse. They are then trapped in the pulse region and have quite large energies.

The nonstationarity of the wave propagation is essential to the electron reflection; and therefore to the acceleration. The large-amplitude pulse with a positive density hump usually has a large electric potential.[29–34] This positive potential can reflect some ions[35] but no electrons. Nonstationary large-amplitude pulses, however, would have small-amplitude, short-wavelength fluctuations;[19] and potential dips could be formed at certain times and locations. Some electrons could be reflected there. (For a more rigorous discussion for the electron reflection,[28] we need to take account of the transverse electric field as well as the longitudinal one.)

In stationary solitary waves with positive density humps,[29–32] such electron reflection would not occur. However, the magnetosonic wave tends to be more nonstationary as the wave-amplitude is increased or the ratio ω_{ce}/ω_{pe} is increased,[19,32,36] where ω_{ce} is the electron cyclotron frequency and ω_{pe} is the electron plasma frequency in an equilibrium state.

In the previous paper,[28] it was analytically shown that the electron acceleration is especially strong at certain propagation angles (the angle between the wave normal and the external magnetic field). However, the theoretical expression for the maximum energy was not given.

In this paper, we analytically estimate the maximum electron energy and compare with simulation results. In Sec. II, on the basis of a two-fluid model, we discuss the structure of an oblique shock wave; we calculate some field quantities and ion fluid momentum. In Sec. III, using these values, we evaluate the maximum energy of reflected electrons. In Sec. IV, by means of a one-dimensional (one space coordinate and three velocity components), relativistic, electromagnetic particle simulation code with full ion and electron dynamics, we further study the shock propagation and electron acceleration. It is found that the theory and simulation are qualitatively in good agreement.

If a strong disturbance is given to a magnetized plasma, then large-amplitude magnetosonic pulses (and other plasma waves) would be excited. These pulses could cause the strong electron acceleration discussed in this paper as well as the ion acceleration discussed in the previous papers.[14–26] In a plasma with a rather strong magnetic field such that $\omega_{ce}/\omega_{pe} \gtrsim 1$, the kinetic energies of the particles thus accelerated can be relativistic.[19,36] Therefore, if large-amplitude magnetosonic pulses (or shock waves) are excited in coronal magnetic tubes in association with solar flares, these pulses

could promptly accelerate ions and electrons to relativistic energies.[3–6]

II. WAVE STRUCTURE

In an oblique magnetosonic shock wave, most of the electrons pass through the shock region without strong acceleration. However, it has been shown recently by particle simulations that some electrons can be reflected and then trapped by the shock wave and that they are accelerated to ultrarelativistic energies.[28] To analytically obtain their energies, we need to know the structure of the shock wave. In this section, we theoretically discuss the nonlinear wave structure on the basis of a two-fluid model and derive some expressions for electromagnetic fields and fluid quantities, which we will use later to evaluate the maximum energy of reflected electrons. [Large-amplitude magnetosonic pulses will be also called shock waves in this paper, because they quickly steepen into (quasi) shock waves.]

We consider a magnetosonic shock wave propagating in the x direction with a velocity $v_{\rm sh}$ ($\partial/\partial y=\partial/\partial z=0$) in an external magnetic field in the (x,z) plane. The angle between the x axis and the magnetic field is denoted by θ. In the theory, we mainly discuss in the wave frame. Because the time derivatives are zero, $\partial/\partial t=0$, in the frame moving with the shock wave, the two-fluid model reads as

$$\frac{d}{dx}(n_j v_{jx})=0, \tag{1}$$

$$m_j n_j v_{jx}\frac{d(\gamma_j \mathbf{v}_j)}{dx}=q_j n_j \mathbf{E}+\frac{q_j}{c} n_j \mathbf{v}_j\times\mathbf{B}, \tag{2}$$

$$\frac{dE_x}{dx}=4\pi e(n_i-n_e), \tag{3}$$

$$\frac{dB_x}{dx}=0, \tag{4}$$

$$\nabla\times\mathbf{E}=0, \tag{5}$$

$$\nabla\times\mathbf{B}=\frac{4\pi}{c}e(n_i\mathbf{v}_i-n_e\mathbf{v}_e), \tag{6}$$

where the subscript j refers to the ions ($j=i$) or electrons ($j=e$); m_j is the mass, n_j is the number density, $\mathbf{v}_j$ is the fluid velocity, c is the speed of light, q_j is the charge ($q_i=e$ and $q_e=-e$), and γ_j is the Lorentz factor,

$$\gamma_j=(1-v_j^2/c^2)^{-1/2}. \tag{7}$$

Equations (1) and (2) represent continuity and momentum equations, respectively, and (3)–(6) are Maxwell equations.

A. Quantities in the upstream region

In the wave frame, the fluid velocities in the far upstream region are given by $\mathbf{v}_{j0}=(-v_{\rm sh},0,0)$. Here, the subscript 0 refers to the quantities in the far upstream region. Equation (1) then gives the density flux as

$$n_j v_{jx}=-n_0 v_{\rm sh}. \tag{8}$$

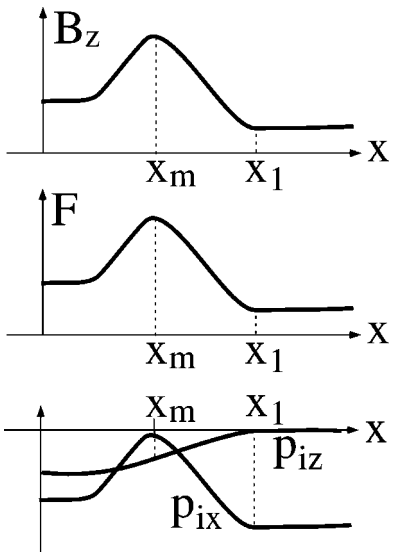

FIG. 1. Schematic diagram of B_z, F, and ion momenta p_{ix} and p_{iz} in the wave frame. The position x_1 indicates the leading edge of the shock wave, and x_m is the point where B_z takes its maximum value.

The density n_0 in the wave frame is related to the density n_{l0} in the laboratory frame through

$$n_0=\gamma_{\rm sh} n_{l0}, \tag{9}$$

where $\gamma_{\rm sh}$ is defined as

$$\gamma_{\rm sh}=(1-v_{\rm sh}^2/c^2)^{-1/2}, \tag{10}$$

and the subscript l indicates the laboratory frame.

From Eq. (4) and the y and z components of Eq. (5), we see that the quantities B_x, E_y, and E_z are constant; $B_x=B_{x0}$, $E_y=E_{y0}$, and $E_z=E_{z0}$. The quantity E_{y0} is given by

$$E_{y0}=-v_{\rm sh}B_{z0}/c, \tag{11}$$

where B_{z0} is related to the laboratory magnetic field B_{lz0} as

$$B_{z0}=\gamma_{\rm sh}B_{lz0}. \tag{12}$$

We choose as $B_{x0}>0$, $B_{z0}>0$, and $E_{y0}<0$. The quantity E_{z0} is zero,

$$E_{z0}=0. \tag{13}$$

Obviously, $B_{lx0}=B_{x0}$, $E_{ly0}=0$, and $E_{lz0}=0$.

B. Maximum value of B_z

The magnetic field becomes much stronger in the shock region than in the upstream region. In particular, B_z has large values in the shock region (see the top panel of Fig. 1). We now obtain the maximum value of B_z.

Adding the x component of Eq. (2) over the particle species and using Eq. (8), we have

$$-n_0 v_{\rm sh}\left(m_i \frac{d(\gamma_i v_{ix})}{dx} + m_e \frac{d(\gamma_e v_{ex})}{dx} \right)$$
$$= e(n_i - n_e)E_x + \frac{e}{c}(n_i v_{iy} - n_e v_{ey})B_z$$
$$- \frac{e}{c}(n_i v_{iz} - n_e v_{ez})B_y . \quad (14)$$

Furthermore, with the aid of Eq. (3) and the y and z components of Eq. (6), we obtain

$$-n_0 v_{\rm sh}\left(m_i \frac{d(\gamma_i v_{ix})}{dx} + m_e \frac{d(\gamma_e v_{ex})}{dx} \right)$$
$$= \frac{1}{4\pi}\left(E_x \frac{dE_x}{dx} - B_z \frac{dB_z}{dx} - B_y \frac{dB_y}{dx} \right). \quad (15)$$

Let the point $x = x_m$ be the position where B_z has its maximum value. Then, integrating Eq. (15) from $x = \infty$ to $x = x_m$, we find

$$-n_0 v_{\rm sh}[m_i \gamma_{im} v_{ixm} + m_e \gamma_{em} v_{exm} + (m_i + m_e)\gamma_{\rm sh} v_{\rm sh}]$$
$$= [E_{xm}^2 - (B_{zm}^2 + B_{ym}^2 - B_{z0}^2)]/(8\pi), \quad (16)$$

where the subscript m refers to the quantities at $x = x_m$. Equation (16) shows a relation between the quantities in the far upstream region and those at $x = x_m$.

Now, following the method of Ref. 36, we obtain B_{zm} from Eq. (16). We assume that the magnitudes of v_{jxm} are much smaller than $v_{\rm sh}$,

$$|v_{jxm}| \ll v_{\rm sh}, \quad (17)$$

and that E_{xm} and B_{ym} are nearly equal to zero,

$$E_{xm} \sim 0, \quad (18)$$

$$B_{ym} \sim 0. \quad (19)$$

We can assume Eq. (17) because the plasma density must be quite high at $x = x_m$; $n_{jm} \gg n_{j0}$. Also, if the magnetic field B_z, the electric potential ϕ, and the z component of the vector potential A_z, have similar profiles, then E_x $(= -d\phi/dx)$ and B_y $(= -dA_z/dx)$ become zero at the position where B_z, ϕ, and A_z take their maximum values, i.e., at $x = x_m$. For small-amplitude magnetosonic waves, we can analytically show that E_x and B_y are proportional to dB_z/dx.[33,34] Strictly speaking, this has not been mathematically proved yet for large-amplitude waves. However, simulations indicate that, even in such waves, E_x and B_y have quite small values at $x = x_m$.[28] Thus, in the theoretical analysis we will assume that the profiles of ϕ and A_z are proportional to $(B_z - B_{z0})$ and hence E_x and B_y are proportional to dB_z/dx; accordingly, we assume Eqs. (18) and (19).

Then, neglecting the terms $m_j \gamma_{jm} v_{jxm}$, E_{xm}^2, and B_{ym}^2 in Eq. (16), we find B_{zm} as

$$B_{zm} = [8\pi n_0 (m_i + m_e)\gamma_{\rm sh} v_{\rm sh}^2 + B_{z0}^2]^{1/2}. \quad (20)$$

In the laboratory frame, we have

$$B_{lzm} = \gamma_{\rm sh}\left(B_{zm} + \frac{v_{\rm sh}}{c} E_{y0} \right). \quad (21)$$

If γ_{em} becomes quite large so that

$$\gamma_{em} \geqslant (m_i/m_e)\gamma_{\rm sh} v_{\rm sh}/|v_{exm}|, \quad (22)$$

then we would not be able to neglect the term $m_e \gamma_{em} v_{exm}$ in Eq. (16). As can be confirmed in the simulations, however, passing electrons (fluid electron) do not have such huge energy. We can therefore neglect this term.

C. Quantity *F*

Let us define a quantity F (Ref. 28) as

$$F = -\int E_\parallel \frac{B}{B_{x0}} dx, \quad (23)$$

where $E_\parallel$ is the electric field parallel to the magnetic field, $E_\parallel = (\mathbf{E}\cdot\mathbf{B})/B$. This will be used when we estimate the z component of the ion momentum and the maximum energy of reflected electrons. In the wave frame, F is calculated as

$$F = \phi + \frac{E_{y0}}{B_{x0}} A_z . \quad (24)$$

Equation (24) indicates that F has a profile similar to ϕ and A_z (and thus to B_z; see the second panel of Fig. 1).

If we also define a function F_l as Eq. (23) using the quantities in the laboratory frame, F and F_l are related as

$$F = \gamma_{\rm sh} F_l . \quad (25)$$

We now calculate the maximum value of F. From the momentum equation for ions, Eq. (2), and the definition of γ_i, Eq. (7), we have an equation for γ_i,

$$m_i c^2 v_{ix} \frac{d\gamma_i}{dx} = eE_x v_{ix} + eE_{y0} v_{iy} . \quad (26)$$

The velocity v_{iy} is obtained from the z component of Eq. (2) as

$$v_{iy} = -\frac{m_i c}{eB_{x0}} v_{ix} \frac{d\gamma_i v_{iz}}{dx} + v_{ix}\frac{B_y}{B_{x0}}. \quad (27)$$

Substituting Eq. (27) to Eq. (26) and integrating from $x = \infty$ to $x = x_m$, we find

$$m_i c^2 (\gamma_{im} - \gamma_{\rm sh}) = -e\left(\phi_m + \frac{E_{y0}}{B_{x0}} A_{zm} \right) - m_i c \frac{E_{y0}}{B_{x0}} \gamma_{im} v_{izm} , \quad (28)$$

where we have chosen as $\phi_0 = 0$ and $A_{z0} = 0$. Combining Eqs. (11), (24), and (28), we obtain the maximum value of F as

$$eF_m = m_i c^2 (\gamma_{\rm sh} - \gamma_{im}) + \frac{B_{z0}}{B_{x0}} v_{\rm sh} p_{izm} , \quad (29)$$

where p_{izm} is the z component of the ion momentum at $x = x_m$, $p_{izm} = m_i \gamma_{im} v_{izm}$. Because $\phi_0 = A_{z0} = 0$, F_0 is zero.

From Eq. (25), we have the maximum value in the laboratory frame as

$$F_{lm} = F_m/\gamma_{\rm sh} . \quad (30)$$

D. Ion momentum p_{iz} at $x=x_m$

Equation (29) shows that we need to estimate the quantities γ_{im} and p_{izm} to calculate the maximum value of eF. However, it is difficult to analytically obtain γ_{im} and p_{izm} for large-amplitude waves in a mathematically rigorous way. Here, we derive their expressions in heuristic terms.

We multiply the ion component of Eq. (2) by $\mathbf{b}/v_{ix}$, where $\mathbf{b}$ is the unit vector given by $\mathbf{b}=\mathbf{B}/B$, and integrate over x from the leading edge of the shock wave, x_1, to x_m. Then, we have

$$\int_{x_1}^{x_m}\mathbf{b}\cdot\frac{d\mathbf{p}_i}{dx}dx=\int_{x_1}^{x_m}\frac{eE_\parallel}{v_{ix}}dx, \tag{31}$$

where $\mathbf{p}_i$ is the ion momentum. To estimate the left-hand side, we use an approximation,

$$\int_{x_1}^{x_m}\mathbf{b}\cdot\frac{d\mathbf{p}_i}{dx}dx\sim\frac{1}{2}(\mathbf{b}_m+\mathbf{b}_0)\cdot(\mathbf{p}_{im}-\mathbf{p}_{i0}). \tag{32}$$

Here, $(\mathbf{b}_m+\mathbf{b}_0)/2$ is a mean value of $\mathbf{b}$, and $\mathbf{p}_{i0}=(-m_i\gamma_{\rm sh}v_{\rm sh},0,0)$. The shock profile just begins to rise at the point $x=x_1$; hence, $\mathbf{b}(x_1)=\mathbf{b}_0$ and $\mathbf{p}_i(x_1)=\mathbf{p}_{i0}$. A schematic diagram for p_{ix} and p_{iz} is shown in the bottom panel of Fig. 1.

As shown by Eq. (17), p_{ix} becomes small in magnitude at the point $x=x_m$. When the ions penetrate the shock region, they are decelerated by the electric potential. Also, a substantial part of the momentum has been converted to the z component by the Lorentz force by the time they reach the point $x=x_m$. We therefore neglect p_{ixm} in Eq. (32) and obtain

$$\int_{x_1}^{x_m}\mathbf{b}\cdot\frac{d\mathbf{p}_i}{dx}dx\sim\frac{1}{2}\left(\frac{B_{zm}}{B_m}+\frac{B_{z0}}{B_0}\right)p_{izm}-\frac{1}{2}\left(\frac{B_{x0}}{B_m}+\frac{B_{x0}}{B_0}\right)p_{ix0}. \tag{33}$$

With the aid of Eq. (8) and Eq. (23), the right-hand side of Eq. (31) can be written as

$$\int_{x_1}^{x_m}\frac{eE_\parallel}{v_{ix}}dx=\frac{eB_{x0}}{n_0v_{\rm sh}}\int_{x_1}^{x_m}\frac{n_i}{B}\frac{dF}{dx}dx. \tag{34}$$

The right-hand side of Eq. (34) is again approximated as

$$\int_{x_1}^{x_m}\frac{n_i}{B}\frac{dF}{dx}dx\sim\left\langle\frac{n_i}{B}\right\rangle\int_{x_1}^{x_m}\frac{dF}{dx}dx. \tag{35}$$

Here, $\langle n_i/B\rangle$ is a mean value of n_i/B and can be estimated by

$$\left\langle\frac{n_i}{B}\right\rangle\sim\frac{1}{2}\left(\frac{n_{im}}{B_m}+\frac{n_0}{B_0}\right). \tag{36}$$

One way of calculating the quantity n_{im}/B_m is given in the Appendix; we may expect that $\langle n_i/B\rangle=(1\sim2)n_0/B_0$. Combining Eqs. (31) to (35), we have

$$\frac{1}{2}\left(\frac{B_{zm}}{B_m}+\frac{B_{z0}}{B_0}\right)p_{izm}-\frac{1}{2}\left(\frac{B_{x0}}{B_m}+\frac{B_{x0}}{B_0}\right)p_{ix0}=e\frac{B_{x0}}{n_0v_{sh}}\left\langle\frac{n_i}{B}\right\rangle F_m. \tag{37}$$

Since p_{ix0} is given by $p_{ix0}=-m_i\gamma_{\rm sh}v_{\rm sh}$, we find p_{izm}, the value at $x=x_m$, as

$$p_{izm}=\frac{-m_i\gamma_{\rm sh}v_{\rm sh}(B_{x0}/B_m+B_{x0}/B_0)+2e[B_{x0}/(n_0v_{\rm sh})]\langle n_i/B\rangle F_m}{(B_{zm}/B_m+B_{z0}/B_0)}. \tag{38}$$

Because we have neglected p_{ixm}, the Lorentz factor γ_{im} can be expressed as

$$\gamma_{im}\sim[1+p_{izm}^2/(m_i^2c^2)]^{1/2}. \tag{39}$$

Here, we have also neglected p_{iym}. Because $dB_z/dx=0$ at $x=x_m$, the plasma current j_y is also zero there. It is therefore expected that v_{iym} and v_{eym} are both small.

We thus have coupled equations, Eqs. (29) and (38), for p_{izm} and F_m. If we Taylor-expand Eq. (39) as

$$\gamma_{im}\sim1+p_{izm}^2/(2m_i^2c^2), \tag{40}$$

then we obtain

$$p_{izm}=\frac{m_iv_{\rm sh}}{a_2}\left\{\left(\frac{B_{z0}}{B_{x0}}a_2-1\right)-\left[\left(\frac{B_{z0}}{B_{x0}}a_2-1\right)^2+2a_2^2\frac{c^2}{v_{\rm sh}^2}(\gamma_{\rm sh}-1)-2\gamma_{\rm sh}a_1a_2\right]^{1/2}\right\}, \tag{41}$$

$$eF_m=m_ic^2\left(\gamma_{\rm sh}-1-\frac{p_{izm}^2}{2m_i^2c^2}\right)+\frac{B_{z0}}{B_{x0}}v_{\rm sh}p_{izm}. \tag{42}$$

Here, we have chosen the negative p_{izm} in Eq. (41). The quantities a_1 and a_2 are defined as

$$a_1=\frac{B_{x0}/B_m+B_{x0}/B_0}{B_{zm}/B_m+B_{z0}/B_0}, \tag{43}$$

$$a_2=\frac{2(B_{x0}/n_0)\langle n_i/B\rangle}{B_{zm}/B_m+B_{z0}/B_0}. \tag{44}$$

Even if we use Eq. (39), instead of Eq. (40), we can solve for p_{izm} and F_m. However, their equations are complicated, and their values are not so different from those given by Eqs. (41) and (42), if $|p_{izm}|/(m_ic)<<1$. The quantity $|p_{izm}|/(m_ic)$ should be smaller than unity as long as the shock speed is much smaller than the speed of light. We thus use Eq. (40) in this paper.

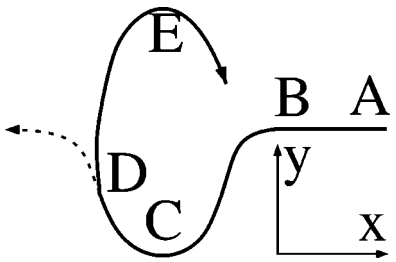

FIG. 2. Schematic diagram of electron guiding-center orbits in the (x,y) plane in the wave frame. Point A is in the upstream region. The x positions of points C and E are $x=x_m$. Passing electrons move as A→B→C→D→dashed line. Some electrons can be reflected at point D and then trapped.

III. MAXIMUM ENERGY OF REFLECTED ELECTRONS

We now discuss ultrarelativistic electrons produced in a shock wave. Large-amplitude shock waves are not perfectly stationary. There are always small-amplitude fluctuations in the profiles of ϕ, B_z, F, etc. If, owing to the fluctuation, the quantity F at a certain time and location becomes smaller than, roughly speaking, its upstream value F_0, then the electrons that have just arrived there would be reflected.[28] Indeed, simulations demonstrate that some of the electrons can be reflected near the end of the main pulse of an oblique shock wave.[27,28] They are then trapped by the shock wave. These electrons have ultrarelativistic energies; their energies are especially high when they are at the point $x=x_m$ where the electric potential ϕ, magnetic field B_z, F, etc. take their maximum values. We show in Fig. 2 a schematic diagram of guiding-center orbits in the (x,y) plane. Point A is in the upstream region; points C and E are at $x=x_m$; and point D is near the end of the main pulse. The trajectory of a passing electron after point D is indicated by the dotted line. The solid line D to E shows the trajectory of a reflected electron.

We estimate the maximum energy of reflected electrons. We again consider in the wave frame. From the equation of motion,

$$m_e \frac{d(\gamma \mathbf{v})}{dt} = -e\mathbf{E} - \frac{e}{c}\mathbf{v}\times\mathbf{B}, \tag{45}$$

we have

$$m_e c^2 \frac{d\gamma}{dt} = -e\mathbf{E}\cdot\mathbf{v}. \tag{46}$$

These are the equations for an electron particle, not for the fluid. The subscript e is omitted for $\mathbf{v}$ and γ. The z component of Eq. (45) gives v_y as

$$v_y = \frac{m_e c}{eB_{x0}} \frac{d(\gamma v_z)}{dt} + v_x \frac{B_y}{B_{x0}}. \tag{47}$$

Using Eq. (47), we eliminate v_y in Eq. (46) to have

$$m_e c^2 \frac{d\gamma}{dt} = -e\left(E_x + \frac{E_{y0}}{B_{x0}} B_y\right) v_x - \frac{E_{y0}}{B_{x0}} m_e c \frac{d(\gamma v_z)}{dt}. \tag{48}$$

Further, we substitute the relations $E_x = -d\phi/dx$, $B_y = -dA_z/dx$, and $v_x = dx/dt$ in Eq. (48) and integrate over time from $t=0$ to $t=t_m$ ($t=0$ is a certain time when the electron is in the far upstream region, and t_m is the time when it reaches the point $x=x_m$ after the reflection near the end of the pulse). With the aid of Eq. (24), we obtain

$$m_e c^2(\gamma_m - \gamma_0) = eF_m - m_e c \frac{E_{y0}}{B_{x0}}(\gamma_m v_{zm} - \gamma_0 v_{z0}). \tag{49}$$

The quantity v_{zm} can be approximated by

$$v_{zm} \sim cB_{zm}/B_m, \tag{50}$$

because the electron velocity should be nearly parallel to the magnetic field at $x=x_m$.[28] We recall that the **E×B** drift speed is rather small there and the electric potential is maximum; hence the electron velocity is relativistic and the parallel component is dominant. The velocity v_{zm} is positive, because reflected electrons are moving back in the positive x direction at $t=t_m$.

From Eqs. (11), (49), and (50), we find the maximum Lorentz factor of a reflected electron as

$$\gamma_m = \frac{eF_m + m_e\gamma_0 c^2 - m_e c(v_{\rm sh}B_{z0}/cB_{x0})\gamma_0 v_{z0}}{m_e c^2[1-(v_{\rm sh}B_{z0}/cB_{x0})(B_{zm}/B_m)]}. \tag{51}$$

It is noted that the denominator in Eq. (51) becomes nearly zero when the shock speed is given by

$$v_{\rm sh}/c \sim (B_{x0}/B_{z0})(B_m/B_{zm}). \tag{52}$$

When the shock speed is around this value, the electron energy γ_m can become especially large.

The maximum value of γ in the laboratory frame is given by the Lorentz transformation as

$$\gamma_{lm} = \gamma_{\rm sh}(1 + v_{xm}v_{\rm sh}/c^2)\gamma_{\rm m} \sim \gamma_{\rm sh}\gamma_{\rm m}. \tag{53}$$

Here, we have neglected the term $v_{xm}v_{\rm sh}/c^2$ in the second equation.

IV. SIMULATION RESULTS

We now use one-dimensional (one spatial coordinate and three velocity components), fully electromagnetic particle code with full ion and electron dynamics[18,37] to investigate the electron acceleration in oblique magnetosonic shock waves. The total grid size is $4096\Delta_g$, where Δ_g is the grid spacing. All lengths and velocities in the simulations were normalized to Δ_g and $\omega_{pe}\Delta_g$, respectively.

We use a bounded plasma model. The plasma is confined in the region $400<x<3696$; at the plasma boundaries, $x=400$ and $x=3696$, the simulation particles are specularly reflected. Outside the plasma region, $0<x<400$ and $3696<x<4096$, electromagnetic radiation is absorbed; hence there is no interaction between the left and right boundaries of the plasma region.

The numbers of simulation particles are $N_i=N_e=262{,}144$. The ion-to-electron mass ratio is $m_i/m_e=100$. The electron cyclotron frequency is $\omega_{ce}/\omega_{pe}=3.0$ in the upstream region. The light speed is $c=4.0$, and the Alfvén speed is $v_{\rm A}=1.2$. The electron and ion thermal velocities are $v_{\rm Te}=0.40$ and $v_{\rm Ti}=0.04$, respectively. The propagation angle θ is 45°.

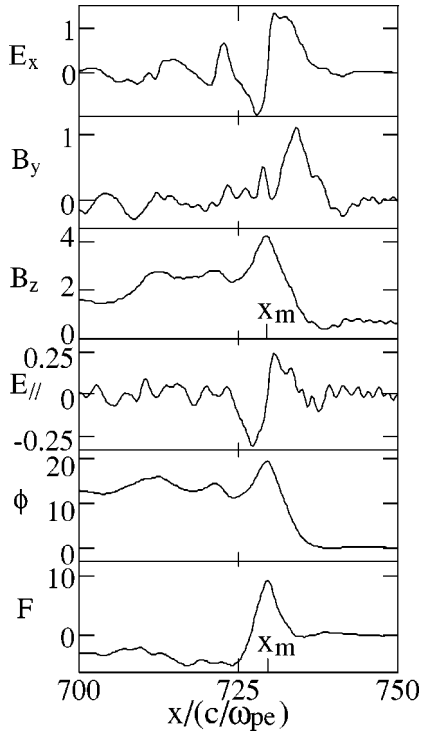

FIG. 3. Snapshots of field profiles at $\omega_{pe}t=900$. Electric and magnetic fields are normalized to B_0, while ϕ and F are normalized to $m_e c^2/e$. The quantities B_z, ϕ, and F take their maximum values at $x=x_m$.

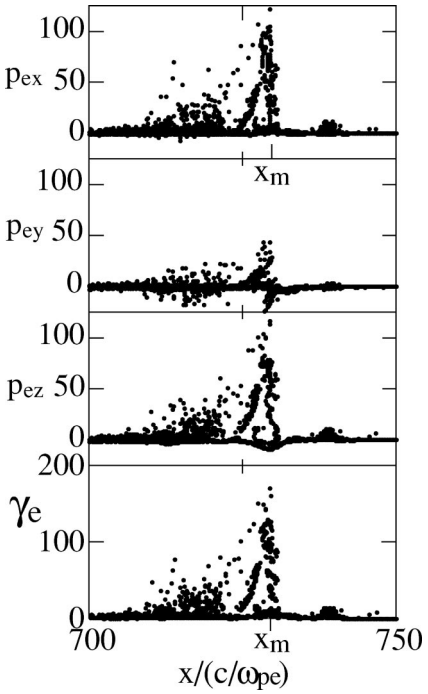

FIG. 4. Phase space plots (x, p_{ex}), (x, p_{ey}), (x, p_{ez}), and (x, γ) of electrons. The momenta are normalized to $m_e c$. High-energy electrons are found at $x \sim x_m$.

The simulation results are shown in the laboratory frame; however, the subscript l is omitted.

We show in Fig. 3 snapshots of field profiles for a shock wave propagating in the positive x direction with a speed $v_{\mathrm{sh}}=2.28v_{\mathrm{A}}$. From the top panel to the bottom one, plotted are the longitudinal electric field E_x, magnetic fields B_y and B_z, electric field $E_\parallel$ parallel to the magnetic field, electric potential ϕ, and quantity F. The fields E_x, B_y, B_z, and $E_\parallel$ are normalized to B_0, and ϕ and F are normalized to $m_e c^2/e$. The potential ϕ was obtained by

$$\phi(x)=-\int^x E_x dx. \tag{54}$$

Figure 3 indicates that, around the point $x=x_m$ where B_z takes its maximum value, ϕ also takes its maximum value, and E_x and B_y are nearly zero. In the main pulse region, the parallel electric field $E_\parallel$ is positive in the region $x_m<x$ and is negative in $x<x_m$. The quantity F therefore takes its maximum value at $x=x_m$. These are consistent with the assumptions made in the theory. (These properties are unchanged if one moves to the wave frame.)

Figure 4 shows phase space plots of electrons (x,p_{ex}), (x,p_{ey}), (x,p_{ez}), and (x,γ_e) in the shock wave. We observe a number of trapped electrons in the main pulse region. They are reflected near the end of the pulse. After the reflection, their p_{ex}, p_{ez}, and γ_e take their maximum values at $x=x_m$. They then reach the shock front region and move back again, relative to the shock wave, with small values of p_{ex}, p_{ez}, and γ_e. Near the end of the main pulse, they are reflected again. They repeat this oscillatory motion; they are trapped. On the other hand, passing electrons pass through the shock region without strong interactions; the assumption in the theory that the term $m_e\gamma_{em}v_{exm}$ in Eq. (16) is small is therefore valid.

Figure 5 displays ion phase space plots. The first and second panels show that the ion orbits are significantly deviated in the shock region, and the fourth panel shows that

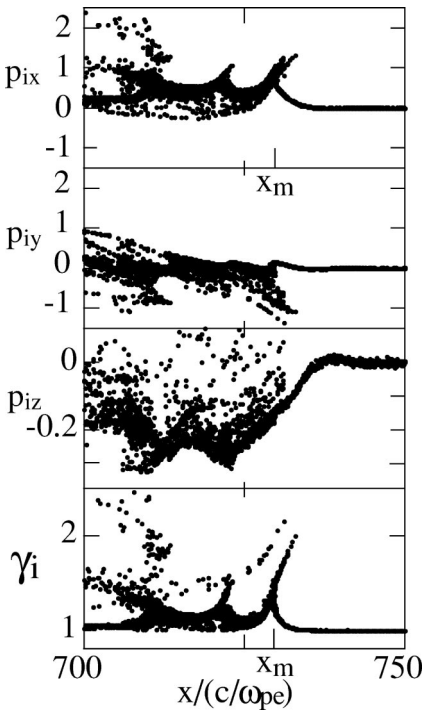

FIG. 5. Phase space plots of ions. The momenta are normalized to $m_i c$. As the ions penetrate the shock region, p_{iz} decreases.

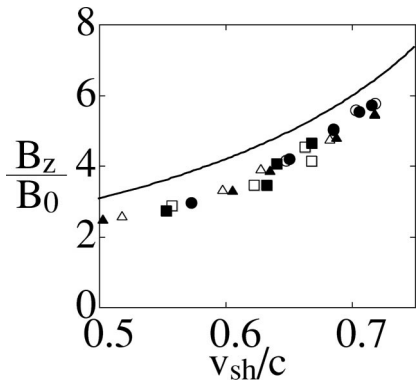

FIG. 6. The maximum value of B_z versus shock speed $v_{\rm sh}$. The solid line shows the theory. The closed and open symbols denote simulation results with $v_{\rm Te}=0.4$ and $v_{\rm Te}=1.5$, respectively. The circles, triangles, and squares show values averaged over time from $\omega_{pe}t=0$ to $\omega_{pe}t=300$, from 300 to 600, and from 600 to 900, respectively.

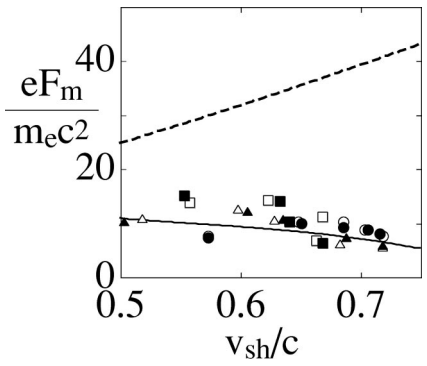

FIG. 8. The maximum value of F versus shock speed $v_{\rm sh}$. The solid line shows the theory. The closed and open symbols denote simulation results with $v_{\rm Te}=0.4$ and $v_{\rm Te}=1.5$, respectively. The circles, triangles, and squares show values averaged over time from $\omega_{pe}t=0$ to $\omega_{pe}t=300$, from 300 to 600, and from 600 to 900, respectively.

some ions are accelerated to energies $\gamma \gtrsim 2.0$. This process is mainly caused by the positive electric potential and was discussed in many papers;[18–20,35–36] thus we will not go into details of this phenomenon. We find in the third panel that, as predicted by the theory, p_{iz} of the bulk ions appreciably decreases in the shock ramp.

In Figs. 6–8, we compare theoretical values of B_{zm}, p_{izm}, and F_m with the simulation results. It will be found that the results of the theory and simulation qualitatively agree. Figure 6 shows the maximum value of B_z as a function of the shock propagation speed $v_{\rm sh}$. To obtain this set of data, we carried out simulations with different values of $v_{\rm sh}$ with other parameters unchanged; $v_{\rm sh}$ was changed by changing the shock amplitude. The solid line represents the theory, B_{lzm} given by Eq. (21). The closed symbols show simulation results with the electron thermal speed $v_{\rm Te}=0.4$; we have also tested the case with $v_{\rm Te}=1.5$, which is shown by the open symbols. (This is also the case in the following figures.) The circles, triangles, and squares show values averaged over time from $\omega_{pe}t=0$ to $\omega_{pe}t=300$, from $\omega_{pe}t=300$ to $\omega_{pe}t=600$, and from $\omega_{pe}t=600$ to $\omega_{pe}t=900$, respectively. We show in Fig. 7 the ion momentum p_{izm} as a function of the shock speed $v_{\rm sh}$. The solid line represents the theory, Eq. (41); here, we have taken $\langle n_i/B\rangle$ as $\sim(1/2)\times(n_{im}/B_m+n_0/B_0)$ and substituted Eq. (A6) in n_{im}. The symbols show the simulation results; the circles, triangles, and squares show the measurements at $\omega_{pe}t=300$, 600, and 900, respectively. We show in Fig. 8 the maximum value of F versus the propagation speed $v_{\rm sh}$. The solid line represents the theory, F_{lm} given by Eq. (30), and the symbols show the simulation results. The meanings of the symbols are the same as those in Fig. 6. For comparison, we show by the curved dotted line the theory given in the previous paper, Eq. (B12) in Ref. 28, in which in the estimation of F_m the z component of the ion velocity, v_{iz}, was neglected compared with v_{ix} at $x=x_m$ in the wave frame. If we neglect p_{izm} in the present theory, Eq. (42), we have a line similar to the dotted curve.

Figure 9 shows the maximum Lorentz factor γ_m of trapped electrons as a function of the shock speed $v_{\rm sh}$. The symbols represent the observed maximum values in the simulations; the closed circles are for $v_{\rm Te}=0.4$ and the open circles are for $v_{\rm Te}=1.5$. The solid line shows the theory, γ_{lm} given by Eq. (53); the third term in the numerator in Eq. (51) was neglected, because it is quite small. The vertical dashed line indicates the shock speed (52), around which the denominator in Eq. (51) takes values close to zero. In both

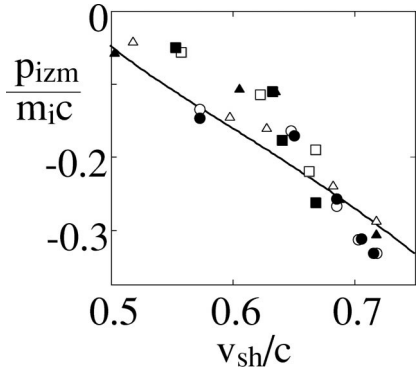

FIG. 7. Ion momentum p_{iz} at $x=x_m$, p_{izm}, versus shock speed $v_{\rm sh}$. The closed and open symbols refer to the results with $v_{\rm Te}=0.4$ and $v_{\rm Te}=1.5$, respectively. The circles, triangles, and squares show measurements at $\omega_{pe}t=300$, 600, and 900, respectively.

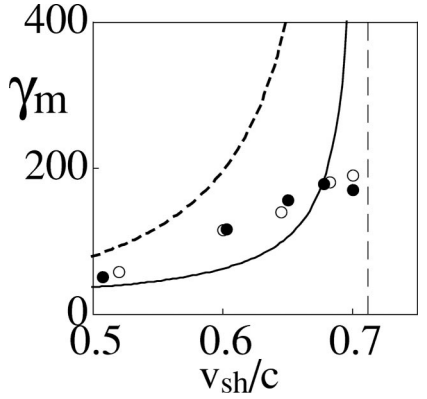

FIG. 9. The maximum Lorentz factor of electrons as a function of the shock speed $v_{\rm sh}$. The closed and open circles show the simulation results for $v_{\rm Te}=0.4$ and $v_{\rm Te}=1.5$, respectively.

theory and simulation, γ_m increases with $v_{\rm sh}$ and has great values near the vertical line. We again show by the curved dotted line the theory given in the previous paper; we substituted the maximum value of F, Eq. (B12) in Ref. 28, in Eq. (51) in the present paper. The theory has been greatly improved.

V. SUMMARY AND DISCUSSION

We have theoretically and numerically studied the structure of magnetosonic shock waves propagating obliquely to a magnetic field and the production of ultrarelativistic electrons by these waves.

First, on the basis of the relativistic two-fluid model, we have analytically obtained the maximum value of the magnetic field B_z in a shock wave. Also, we have calculated the ion momentum p_{iz} at the point x_m where B_z has its maximum value. We then estimated the maximum value of the quantity F. Using these values, we found the maximum energy of the electrons that are trapped in the shock region.

Next, we used a one-dimensional, relativistic, electromagnetic particle code with full ion and electron dynamics to investigate the shock propagation and electron acceleration in a self-consistent manner. We have compared the theoretical estimates for the wave quantities and the maximum electron energy with the simulation results. The theory and simulation were qualitatively in good agreement.

The theory for the maximum electron energy has been greatly improved. However, it still has some limitations. For instance, we have neglected the effect of B_y on the particle motion. In a small-amplitude wave, B_y is much smaller in magnitude than B_{x0} and B_z.[29–34] However, the simulations show that in large-amplitude waves it is not very small; Fig. 3 indicates that the maximum value of B_y is about 25% that of B_z. Hence, B_y may give some influence on the particle motion. The influence of B_y may be even more significant in the waves with much larger amplitudes than the waves in the present simulations. The effect of trapped electrons may also be important. Electron trapping takes place when F becomes small in the end of a large pulse. The number of trapped electrons can thus increase with time, and it can be comparable to the number of passing electrons in the pulse region. These trapped electrons could affect the wave structure and could change values of F. This would modify the maximum value of electron energy. Further development of the quantitative theory of large-amplitude waves is desired.

APPENDIX: MAXIMUM VALUE OF ION DENSITY

For small-amplitude waves, one can analytically find relations among physical quantities.[33,34] However, for large-amplitude oblique magnetosonic waves, it is quite difficult to do it in a mathematically rigorous way. We here show one heuristic way of estimating n_{im}/B_m.

As we have mentioned, the z component of the magnetic field predominates over other magnetic components in the shock region, if the wave amplitude is large. The shock structure thereby becomes similar to that of a quasi-perpendicular shock wave. Hence we apply the theory for large-amplitude perpendicular shock waves[36] to estimate n_{im}/B_m.

The electron velocity v_{ex} is quickly decreased in magnitude in the shock region if the electrons move with **E×B** drift; note that E_y is constant in the wave frame and **B** is strong in the shock region. In a quasi-perpendicular shock wave,[36] the electron density is given by

$$n_e=(B/B_0)n_0. \tag{A1}$$

It increases with an increasing magnetic field.

On the other hand, because the ions have great inertia, they are not quickly decelerated when they enter the shock region. The difference between the electron and ion motions produces a large electric potential ϕ. This potential will then significantly decelerate the ions. Let Δ be the width of the shock ramp; thus, $x_1=x_m+\Delta$ is the leading edge of the shock wave (see Fig. 1). Roughly speaking, we can assume that, in the region $x_m+\Delta/2<x<x_m+\Delta$, the change in the ion density is rather small,

$$n_i\sim n_0, \tag{A2}$$

while, as one moves from $x=x_m+\Delta/2$ to $x=x_m$, n_i increases rather rapidly to n_{im};[36] therefore, n_i may be approximated by

$$n_i\sim n_0-(n_{im}-n_0)[x-(x_m+\Delta/2)]/(\Delta/2), \tag{A3}$$

for $x_m<x<x_m+\Delta/2$.

Because the values of E_x at $x=x_m$ and at $x=x_m+\Delta$ are both zero, it follows from Gauss' law (3) that

$$0=\int_{x_m}^{x_m+\Delta} n_i dx-\int_{x_m}^{x_m+\Delta} n_e dx. \tag{A4}$$

For the density profiles assumed above, Eq. (A4) gives

$$0=[(n_{im}+n_0)/2](\Delta/2)+n_0(\Delta/2)-[(n_{em}+n_0)/2]\Delta. \tag{A5}$$

From Eqs. (A1) and (A5), we find the maximum ion density n_{im} as

$$\frac{n_{im}}{B_m}=2\frac{n_0}{B_0}-\frac{n_0}{B_m}, \tag{A6}$$

which indicates that n_{im}/B_m is around $2n_0/B_0$.

[1] T. Tajima and J. M. Dawson, Phys. Rev. Lett. **43**, 267 (1979).
[2] C. Joshi, C. E. Clayton, W. B. Mori, J. M. Dawson, and T. Katsouleas, Comments Plasma Phys. Control. Fusion **16**, 65 (1994).
[3] E. L. Chupp, H. Debrunner, E. Flückiger *et al.*, Astrophys. J. **318**, 913 (1987).
[4] D. J. Forrest and E. L. Chupp, Nature (London) **305**, 291 (1983).
[5] H. Nakajima, T. Kosugi, K. Kai, and S. Enome, Nature (London) **305**, 292 (1983).
[6] S. R. Kane, E. L. Chupp, D. J. Forrest, G. H. Share, and E. Rieger, Astrophys. J. Lett. **300**, L95 (1986).
[7] K. Koyama, R. Petre, E. V. Gotthelf *et al.*, Nature (London) **378**, 255 (1995).
[8] T. Tanimori, Y. Hayami, S. Kamei *et al.*, Astrophys. J. Lett. **497**, L25 (1998).
[9] T. Tanimori, K. Sakurazawa, S. A. Dazeley *et al.*, Astrophys. J. Lett. **492**, L33 (1998).
[10] E. Fermi, Phys. Rev. **75**, 1169 (1949).
[11] R. D. Blandford and D. Eichler, Phys. Rep. **154**, 1 (1987).

[12]S. P. Reynolds and D. C. Ellison, Astrophys. J. **399**, L75 (1992).
[13]J. E. Gunn and J. P. Ostriker, Phys. Rev. Lett. **22**, 728 (1969).
[14]D. Biskamp and H. Welter, Nucl. Fusion **12**, 663 (1972).
[15]M. M. Leory, D. K. Winske, C. C. Goodrich, C. S. Wu, and K. Papadopoulos, J. Geophys. Res. **87**, 5081 (1982).
[16]D. W. Forslund, K. B. Quest, J. U. Brackbill, and K. Lee, J. Geophys. Res. **89**, 2142 (1984).
[17]B. Lembege and J. M. Dawson, Phys. Fluids B **1**, 1001 (1989).
[18]Y. Ohsawa, Phys. Fluids **28**, 2130 (1985).
[19]Y. Ohsawa, J. Phys. Soc. Jpn. **55**, 1047 (1986).
[20]Y. Ohsawa, J. Phys. Soc. Jpn. **59**, 2782 (1990).
[21]R. Z. Sagdeev and V. D. Shapiro, Zh. Eksp. Teor. Fiz. Piz'ma Red. **17**, 387 (1973) [JETP Lett. **17**, 279 (1973)].
[22]M. A. Lee, V. D. Shapiro, and R. Z. Sagdeev, J. Geophys. Res. **101**, 4777 (1996).
[23]M. Toida and Y. Ohsawa, J. Phys. Soc. Jpn. **64**, 2038 (1995).
[24]M. Toida and Y. Ohsawa, Sol. Phys. **171**, 161 (1997).
[25]K. Maruyama, N. Bessho, and Y. Ohsawa, Phys. Plasmas **5**, 3257 (1998).
[26]T. Masaki, H. Hasegawa, and Y. Ohsawa, Phys. Plasmas **7**, 529 (2000).
[27]N. Bessho, K. Maruyama, and Y. Ohsawa, J. Phys. Soc. Jpn. **68**, 1 (1999).
[28]N. Bessho and Y. Ohsawa, Phys. Plasmas **6**, 3076 (1999).
[29]J. H. Adlam and J. E. Allen, Philos. Mag. Suppl. **3**, 448 (1958).
[30]L. Davis, R. Lüst, and A. Schlüter, Z. Naturforsch. A **13**, 916 (1958).
[31]C. S. Gardner and G. K. Morikawa, Commun. Pure Appl. Math. **18**, 35 (1965).
[32]Y. Ohsawa, Phys. Fluids **29**, 2474 (1986).
[33]T. Kakutani, H. Ono, T. Taniuti, and C. C. Wei, J. Phys. Soc. Jpn. **24**, 1159 (1968).
[34]Y. Ohsawa, Phys. Fluids **29**, 1844 (1986).
[35]Y. Ohsawa, J. Phys. Soc. Jpn. **59**, 2782 (1990).
[36]S. Nakazawa and Y. Ohsawa, J. Phys. Soc. Jpn. **66**, 2044 (1997).
[37]P. C. Liewer, A. T. Lin, J. M. Dawson, and M. Z. Caponi, Phys. Fluids **24**, 1364 (1981).